Visions and Strategies for Reinforcing Additively Manufactured Constructions 2023

Conference paper

https://doi.org/10.52825/ocp.v3i.759

Published: 15 Dec. 2023

Fiber Reinforcement of 3D Printed Concrete by Material Extrusion Toolpaths Aligned to Principal Stress Trajectories

Daniel Auer[1] [https://orcid.org/0000-0002-9701-7807], Mohammad Olabi[1] [https://orcid.org/0009-0007-7694-0751], Freek Bos[1] [https://orcid.org/0000-0002-6666-2395] and Oliver Fischer[1] [https://orcid.org/0000-0003-0528-5634]

[1] Chair of Concrete and Masonry Structures,School of Engineering and Design, Technical University of Munich,

Correspondance: daniel.auer@tum.de

Abstract. Additive manufacturing of cementitious materials is a rapidly growing branch of manufacturing both in research and industry, particularly the variant of material deposition by extrusion. This process results in a strong anisotropy in mechanical properties, owing largely to the interfaces between adjacent filaments. This anisotropy is even more pronounced when fiber reinforced mortars or continuous entrained reinforcement components such as cables are used. To exploit orientation-dependent performance, the print path can be designed to align with the principal (tensile) stress trajectories. However, obtaining an appropriate print path based on this concept poses several challenges, related to the filling of intermediate spaces between two trajectories. In this paper, an approach for planning such a robot toolpath is presented, elaborated, and illustrated by means of a case study on a well-known reference case. The main features of the tool planning method are the relaxation of the offset width, the avoidance of toolpaths with acute angles by intersecting offset curves, and a continuous toolpath.

Keywords: Additive Manufacturing, Structural Design, 3D Concrete Printing, Fiber Reinforced Concrete, Carbon Fiber, Principal Stress Trajectories

1. Introduction

Research into extrusion-based additive manufacturing of concrete, commonly known as 3D concrete printing (3DCP), is rapidly expanding due to the promising potential of the technology, including the possibility of producing geometrically intricate and non-repetitive elements at practically no additional cost [1]. However, although 3DCP allows considerably more geometrical freedom than conventional casting of concrete, its possibilities are primarily defined by two constraints that originate in the nature of the process. First, the variations in the z-direction are limited because there is usually no support material as can be found in some other additive manufacturing processes such as particle bed binding processes and the more recently introduced method of injection 3D concrete printing [2, 3]. Second, the material is typically deposited in continuous filaments (even though some facilities have functionalities to stop and restart the material flow with a secondary material extruder at the print head, this cannot be done in a resolution that really allows to move away from geometries dominated by continuous filaments). These constraints largely dictate the appearance of 3D printed concrete elements, which, although they are used in a variety of different applications, are characterized by printed wall segments consisting of vertically stacked layers, with a more or less consistent geometry over the height and arbitrary shapes in the horizontal print plane.

Mainly due to the deposition in continuous filaments, 3D-printed concrete exhibits strongly anisotropic behavior caused by the interfaces between filaments. This anisotropy is particularly pronounced under tension [4–9]. Considering that tensile strength is usually ignored in structural concrete engineering anyway due to its brittle failure behavior, one might consider this of minor relevance. However, practically all the hitherto proposed reinforcement solutions for printed concrete are likewise governed by the filament deposition and are effective either in the u-direction (i.e., parallel to the print path) or the perpendicular directions (v and w) [10]. The u, v, w notation is a local coordinate system for describing the orientation of the print path, which is used to characterize the anisotropy [11]. Thus, reinforcement options for printed concrete are also highly defined by the direction of the print path.

Several of the 3DCP reinforcement options with the least impact on the flexibility of the 3DCP process are largely or even only effective in the u-direction. This includes solutions based on adding short fibers to the cementitious matrix. Their orientation, and thus the performance of the fiber-reinforced material, is strongly dependent on the flow behavior of the material during deposition and the geometry characteristics of the print nozzle. Generally, fibers thus tend to orientate in the u- or u/v-direction [12, 13]. Considering, however, that short fibers are hardly effective across interfaces between layers, fiber-reinforced printed concrete tends to exhibit significantly higher tensile strength and ductility in the u-orientation than in the v- and w-orientation. Such anisotropic effects are even more pronounced when continuous tensile components are introduced in the print filament, such as cables, or glass- or carbon fiber yarn [14–17].

To optimally exploit the structural capacities of such reinforcement concepts, the geometrical flexibility of the 3DCP process can be employed. Rather than designing an orthogonal reinforcement layout, as it is standard in conventional reinforced concrete, in printed concrete, the filament can follow the orientation of the principal tensile stress trajectories. In beams, this might even obviate the need for separate shear reinforcement in addition to main bending reinforcement since no other tensile components remain when the principal tensile stress directions are reinforced. Considering the limitations of most of the current extrusion-based 3DCP facilities, this strategy could be applied to elements that are printed in a flat or curved u, v-plane.

Obtaining a suitable print path, however, remains a challenge. First, Finite Element Analysis (FEA), used to derive principal stress distributions, typically delivers stress data in points, not in continuous lines. Furthermore, since stress trajectories are not equidistant throughout a computational domain, filling up the intermediate space between them is not apparent, particularly when this must be done using a continuous print path. This paper presents a method to automatically generate an appropriate continuous print path from principal stress data from FEA that can be used to print optimized structural elements.

2. Computational Methods

2.1 Methods of Principal Stress-Aligned Structures

Additive manufacturing (AM) revolutionizes the way materials are strategically structured, offering unprecedented control over the orientation of fibers in composite materials like fiber-reinforced concretes. Traditional manufacturing methods often limit fiber alignment to simple configurations, usually parallel or perpendicular to the plane of the material; see reinforced concrete slabs, for example. However, additive manufacturing allows for the precise deposition of fibers along paths that can be aligned to the principal stresses experienced by the structure in its final application. This targeted alignment enhances material properties like strength, stiffness, and fatigue resistance, enabling the creation of not only lighter but also more efficient and durable components, thus pushing the boundaries of material science and engineering.

The surge in computing power, coupled with the growing importance of sustainable manufacturing, has paved the way for innovative toolpath generation methods to optimize the additive manufacturing process for greater resource efficiency and better material properties. The most recent works in this field of research are given in [18–26], primarily treating non-cementitious materials. In the context of 3DCP, the works of Blagojevic [27], Breseghello [28, 29], Dörrie [30], and Liu [31] deal with toolpath planning and principal stress trajectories. Most works previously mentioned typically employ principal stress trajectories as the direct basis for toolpaths, resulting in gaps within the computational domain. These gaps can alter the structural behavior. Alternatively, some works use a uniform angle for an entire layer. The algorithm described here effectively fills the entire computational domain with curvilinear toolpaths.

2.2 Finite Element Simulations as a Basis for Principal Stress Trajectories

Due to nonlinear material behavior and increasingly complex geometries, finite element simulations are used instead of analytical solutions to determine loaded structures' stress and deformation responses. However, this greater flexibility comes with an increased cost to determine the stresses at any location in the computational domain Ω.

Starting from an arbitrary initial point x_k, z_k with $k = 0$, the stresses must be determined first. In the plane stress state, these are $\sigma_{xx}(x_k, z_k)$, $\sigma_{zz}(x_k, z_k)$, and $\sigma_{xz}(x_k, z_k)$. From this, the principal stress direction $\varphi(x_k, z_k)$ acc. Eq. (1) can be determined.

$$\varphi(x_k, z_k) = 0.5 \cdot \arctan\left(\frac{2 \cdot \sigma_{xz}(x_k, z_k)}{\sigma_{zz}(x_k, z_k) - \sigma_{xx}(x_k, z_k)}\right) \tag{1}$$

A simple but not optimal method for trajectory determination is the explicit one-step method by Euler, as shown in Eqs. (2) and (3). The accuracy depends strongly on the selected step size Δt. Usually, multi-step methods with adaptive step size control are used.

$$x_{k+1} = x_k \pm \Delta s \cdot \Delta t \cdot \underbrace{\cos\left(\varphi(x_k, z_k)\right)}_{\Delta x_k} \tag{2}$$

$$z_{k+1} = z_k \pm \Delta s \cdot \Delta t \cdot \underbrace{\sin\left(\varphi(x_k, z_k)\right)}_{\Delta z_k} \tag{3}$$

If determining the principal stress direction is interpreted as the solution of an eigenvalue problem, the principal stress direction corresponds to an eigenvector. However, eigenvectors have the property of being ambiguous. In the case of the determination of principal stress trajectories, this means that the negative eigenvector is also an eigenvector. This leads to the principal stress trajectory deviating from the correct solution, and strong oscillations occur. By comparing two consecutive principal directions in their vectorial forms $(\Delta x_k, \Delta x_{k-1}, \Delta z_k, \Delta z_{k-1})$ the correction factor Δs acc. Eq. (4) can be determined.

$$\Delta s = \begin{cases} +1 & \text{if } \Delta x_{k-1} \cdot \Delta x_k + \Delta z_{k-1} \cdot \Delta z_k > 0 \\ -1 & \text{else} \end{cases} \tag{4}$$

The previous calculations are performed until the next point x_{k+j}, z_{k+j} is outside the computational domain Ω. Then the trajectory is determined starting from the initial point in the other direction and merged to the final trajectory. Figure 1 shows the first principal stress trajectories with randomly chosen initial points for a common structural system.

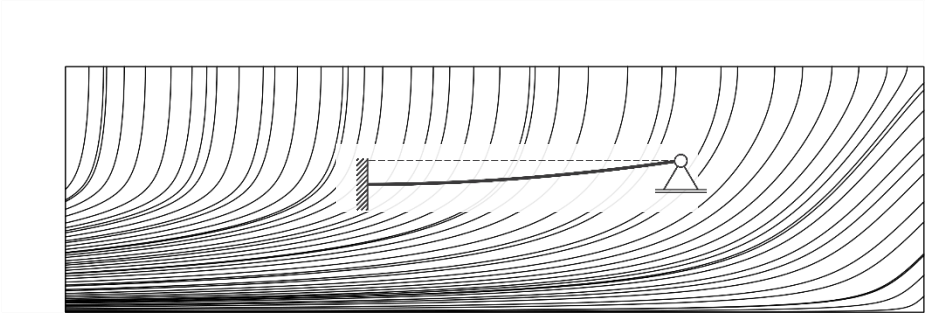

Figure 1: 1st principal (tensile) stress trajectories for a beam with the following boundary conditions: on the left side, a unit vertical displacement of 1, a constrained rotation of 0, and on the right side, a constrained vertical displacement of 0 and an unconstrained rotation, as illustrated in the subfigure. The loading equals the symmetric half of a roller-supported beam with a three-point bending loading. The dimensions of the computational domain Ω are 3500 mm in length and 1000 mm in height.

3 Print Paths between Two Principal Stress Trajectories – Naïve Approach

Figure 1 clearly shows that two adjacent principal stress trajectories are not equidistant throughout the computational domain Ω, see the distribution along the top and left edges. This chapter briefly demonstrates which problems arise when trying to fill the area between two adjacent principal stress trajectories T_A and T_B completely. This is illustrated in Figure 2 and Figure 3. For this purpose, a nominal nozzle width w_{nom} of 16 mm is assumed. The next chapter shows an optimized approach.

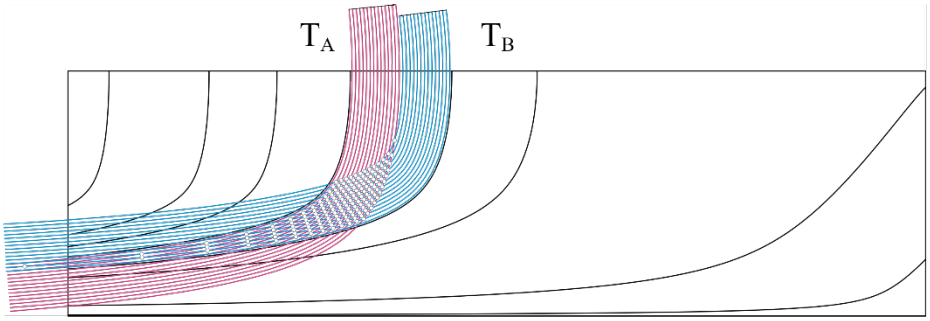

Figure 2: Offsetting two principal stress trajectories by 16mm toward the other principal stress trajectory. T_A (pink) is offset towards T_B (blue) and T_B towards T_A. Figure 2 is equal to Figure 1 with a reduced number of trajectories.

If the offset curves are naïvely intersected, a multitude of sharp angles remain as well as a gap, that this approach cannot fill (Figure 3). The disadvantage of sharp angles is that the print paths are spaced less than the nominal filament width w_{nom} over longer distances, resulting in toolpath-induced over-extrusion in 3DCP. If one looks at the dimensions of the gap on the top side, we see that it is smaller than $2 \cdot w_{nom}$ with 30.19 mm. Thus, no offset curves intersect, and a gap is created unless further measures are taken. If toolpaths are added here anyway, a local over-extrusion occurs compared to the rest of the surface between the trajectories.

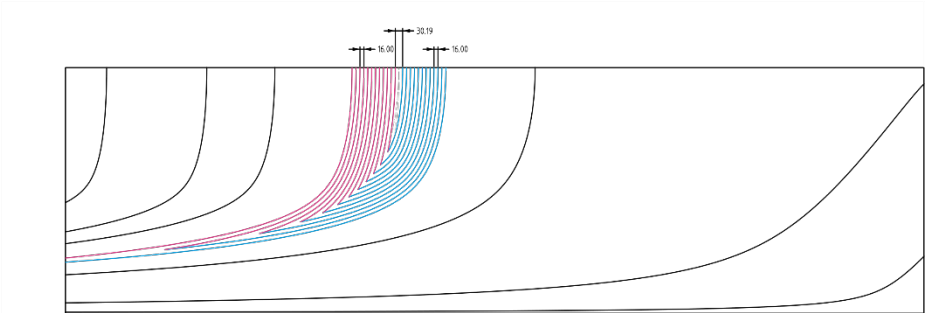

Figure 3: Result of path planning with the naïve approach. The occurrence of a gap, sharply angled toolpaths, and the fact that the toolpath ends again at the same side where it was started is strongly dependent on $d_{max}(T_A, T_B)$ with 414.19 and cannot be influenced. The gap with 30.19 mm is created by evaluating the expression $d_{max}(T_A, T_B)\ mod\ 2 \cdot w_{nom} = 414.19\ mod\ 2 \cdot 16 = 30.19$.

4. Print Paths between Two Principal Stress Trajectories – Optimized Approach

The improved approach proposed in this paper targets the previously mentioned flaws. The sharply converging toolpaths are reduced by sidestepping to the offset curves of the adjacent trajectory and are locally limited. On the other hand, by adjusting the nozzle width to an effective value, gaps are prevented from occurring, as seen in Figure 9. The toolpath is planned with a nozzle width $\mathrm{w_{eff}} \leq \mathrm{w_{nom}}$, which ensures complete filling of the area between two trajectories. $\mathrm{w_{eff}} \leq \mathrm{w_{nom}}$ results in almost everywhere uniform over-extrusion to a reasonable extent (~15%), whereby better interlayer bond properties within the plane can be expected.

The effective nozzle width $\mathrm{w_{eff}}$ can be computed by determining the maximum distance $\mathrm{d_{max}(T_A, T_B)}$ between two adjacent principal stress trajectories $\mathrm{T_A}$ and $\mathrm{T_B}$ and performing an integer division on the half distance $\dot{\mathrm{d}}$ acc. Eq. (5) by the nominal nozzle width $\mathrm{w_{nom}}$. Eq. (6) gives n, which is the total number of necessary offset curves of each $\mathrm{T_A}$ and $\mathrm{T_B}$.

$$\dot{\mathrm{d}} = \frac{\mathrm{d_{max}(T_A, T_B)}}{2} \tag{1}$$

$$\mathrm{n} = \left\lfloor \frac{\dot{\mathrm{d}}}{\mathrm{w_{nom}}} \right\rfloor + 1 \tag{2}$$

The reason for the addition of 1 is that the effective nozzle width $\mathrm{w_{eff}}$ and thus the offset of the extrusion paths is always smaller than the nominal nozzle width $\mathrm{w_{nom}}$, thus one additional offset curve is required to ensure that no gaps remain between adjacent extrusion paths.

If n is an odd integer, it is recommended to add another 1 to get an even integer, as outlined in Eq. (7). The reason for this can be taken from Figure 4. If a tool traverses an even number of offset curves, the path ends on the same side where it started, increasing planning reliability. In the naïve approach of the previous chapter, this was also not addressed.

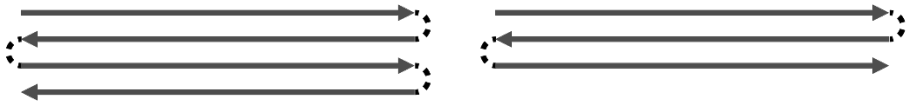

Figure 4: Effect of even and odd numbers of offset curves on toolpaths' start and endpoints. The start and end points are on the same side for even numbers. For odd numbers, they are on different sides.

$$\dot{n} = \begin{cases} n & \text{if n is even} \\ n+1 & \text{if n is odd} \end{cases} \tag{3}$$

Finally, with Eq. (8) the effective nozzle width w_{eff} can be computed by dividing the half distance $\dot{d}$ by the even number $\dot{n}$ of offset curves with which the $\dot{n}$ offset curves are generated.

$$w_{eff} = \frac{\dot{d}}{\dot{n}} \tag{4}$$

All computations are illustrated with Figure 5.

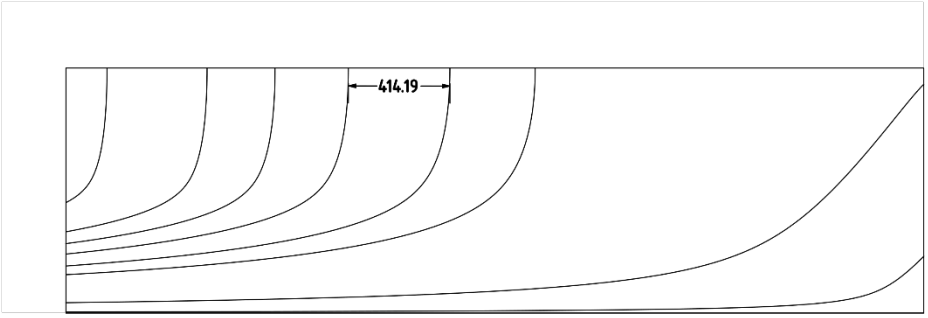

Figure 5: $d_{max}(T_A, T_B)$ is 414.19 mm, resulting in $\dot{d}$ = 207.095 mm, resulting in n = 13, resulting in $\dot{n}$ = 14 and w_{eff} = 207.095/14 = 14.7925 mm

With the help of the counting variable $i \in [0, \dot{n} - 1]$, the magnitudes $o_A(i)$ and $o_B(i)$ of the i^{th} offset curve of both T_A and T_B are computed. Table 1 shows, depending on the layer, different strategies to minimize the cavities between the layers in w-direction by shifting the offset curves by half a filament width. For $\dot{n}$ = 14 and w_{eff} = 14.7925 the 13 offsets of T_A would be $o_A(i) = [7.40 \quad 22.19 \quad \dots \quad 184.91 \quad 199.70]$.

Table 1: Overview of parallel offset strategies per layer (briefly visualized in top left) to achieve an offset of the toolpath of half a filament width between vertical layers to minimize cavities in ***w***-direction.

	Layer I	Layer II

	$o_A(i) = +\left(\frac{w_{eff}}{2} + i \cdot w_{eff}\right)$
Offset of trajectory T_A	$o_A(i) = +(w_{eff} + i \cdot w_{eff})$
	$o_B(i) = -\left(\frac{w_{eff}}{2} + i \cdot w_{eff}\right)$
Offset of trajectory T_B	$o_B(i) = -(0 + i \cdot w_{eff})$

The following part of the methodology deals only with the intersecting subset $\ddot{n} = 13$ of the $\dot{n} = 14$ offset curves. Figure 9 shows the final output, which is derived based on a schematic illustration of Figure 6, shown in Figure 7. Figure 8 corresponds to Figure 9, only the curve segments were straightened, and the intersections were arranged on a regular grid.

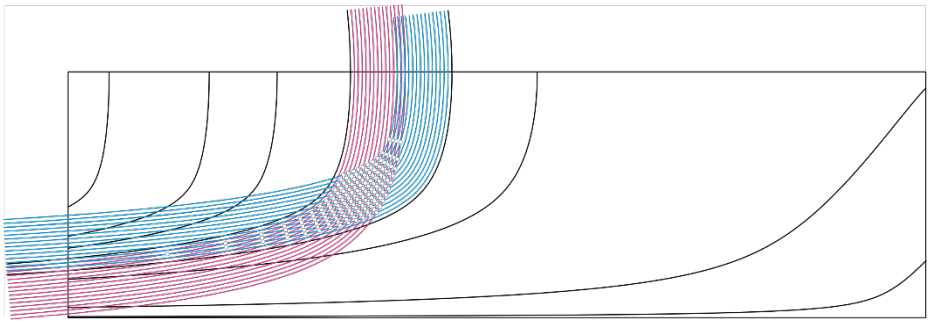

Figure 6: Both trajectories T_A and T_B are offset $\dot{n}$ times in the direction of the other trajectories. Note, that only a subset $\ddot{n} \leq \dot{n}$ of the offset curves intersect. In this example only $\ddot{n} = 13 \leq \dot{n} = 14$ curves intersect. The trajectories T_A and T_B have been extended on both sides for better visualization. $o_A(i)$ and $o_B(i)$ are computed with strategy "Layer I".

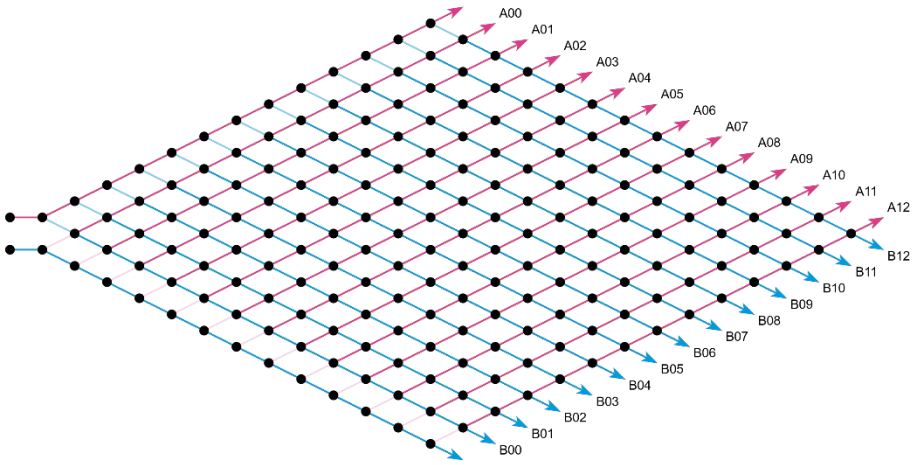

Figure 7: Schematic representation of the offset curves, where only intersecting offset curves are assigned a number. The black points correspond to an intersection, A_j corresponds to the j^{th} intersecting offset curve of T_A. The same holds for B and T_B.

The generating functions $g_A(k)$ and $g_B(k)$ acc. Eqs. (9) and (10) construct a series of integers for $0 \leq k \leq \ddot{n} - 1 = 13$, which determine, which segment between two intersections along an offset-curve needs to be deleted. The results of $g_A(k)$ and $g_B(k)$ can be converted into a pattern, analogous to Table 2, by simply filling the $g_A(k)$ or $g_B(k)$ first rows with 1. This forms the basis of a continuous toolpath with minimal over-extrusion and no remaining gaps.

$$g_A(k) = \begin{cases} 0 & \text{if } k = 0 \\ k & \text{if } k \text{ is odd and } 1 \leq k \leq ï - 2 \\ k - 2 & \text{if } k \text{ is even and } 1 \leq k \leq ï - 2 \\ n - 1 & \text{if } k = ï - 1 \end{cases} \quad (5)$$

$$g_B(k) = \begin{cases} 0 & \text{if } k = 0 \\ k + 2 & \text{if } k \text{ is odd and } 1 \leq k \leq ï - 2 \\ k & \text{if } k \text{ is even and } 1 \leq k \leq ï - 2 \\ n - 1 & \text{if } k = ï - 1 \end{cases} \quad (6)$$

Table 2: The rows of the table indicate the offset curves A_j and B_j, respectively, and the columns indicate the segments between the intersections with B_k and B_{k+1} and A_k and A_{k+1}, respectively, that should be removed (0) or preserved (1) so that the desired pattern can be obtained. For clarity of orientation, the segment between the intersections with A_{10} and A_{11} of curve B_{01} was marked in green. The first and last columns represent the areas before and after the last intersection.

	B_{00}	B_{00} - B_{01}	B_{01} - B_{02}	B_{02} - B_{03}	B_{03} - B_{04}	B_{04} - B_{05}	B_{05} - B_{06}	B_{06} - B_{07}	B_{07} - B_{08}	B_{08} - B_{09}	B_{09} - B_{10}	B_{10} - B_{11}	B_{11} - B_{12}	B_{12}		A_{00}	A_{00} - A_{01}	A_{01} - A_{02}	A_{02} - A_{03}	A_{03} - A_{04}	A_{04} - A_{05}	A_{05} - A_{06}	A_{06} - A_{07}	A_{07} - A_{08}	A_{08} - A_{09}	A_{09} - A_{10}	A_{10} - A_{11}	A_{11} - A_{12}	A_{12}
A_{00}	0	1	1	1	1	1	1	1	1	1	1	1	1	1	B_{00}	0	1	0	1	1	1	1	1	1	1	1	1	1	1
A_{01}	0	1	1	1	1	1	1	1	1	1	1	1	1	1	B_{01}	0	0	0	1	1	1	1	1	1	1	1	1	1	1
A_{02}	0	1	0	1	1	1	1	1	1	1	1	1	1	1	B_{02}	0	0	0	1	0	1	1	1	1	1	1	1	1	1
A_{03}	0	0	0	1	1	1	1	1	1	1	1	1	1	1	B_{03}	0	0	0	0	0	1	1	1	1	1	1	1	1	1
A_{04}	0	0	0	1	0	1	1	1	1	1	1	1	1	1	B_{04}	0	0	0	0	0	1	0	1	1	1	1	1	1	1
A_{05}	0	0	0	0	0	1	1	1	1	1	1	1	1	1	B_{05}	0	0	0	0	0	0	0	1	1	1	1	1	1	1
A_{06}	0	0	0	0	0	1	0	1	1	1	1	1	1	1	B_{06}	0	0	0	0	0	0	0	1	0	1	1	1	1	1
A_{07}	0	0	0	0	0	0	0	1	1	1	1	1	1	1	B_{07}	0	0	0	0	0	0	0	0	0	1	1	1	1	1
A_{08}	0	0	0	0	0	0	0	1	0	1	1	1	1	1	B_{08}	0	0	0	0	0	0	0	0	0	1	0	1	1	1
A_{09}	0	0	0	0	0	0	0	0	0	1	1	1	1	1	B_{09}	0	0	0	0	0	0	0	0	0	0	0	1	1	1
A_{10}	0	0	0	0	0	0	0	0	0	1	0	1	1	1	B_{10}	0	0	0	0	0	0	0	0	0	0	0	1	0	1
A_{11}	0	0	0	0	0	0	0	0	0	0	0	1	1	1	B_{11}	0	0	0	0	0	0	0	0	0	0	0	0	0	1
A_{12}	0	0	0	0	0	0	0	0	0	0	0	1	0	1	B_{12}	0	0	0	0	0	0	0	0	0	0	0	0	0	1
k	0	1	2	3	4	5	6	7	8	9	10	11	12	13	k	0	1	2	3	4	5	6	7	8	9	10	11	12	13
$g_A(k)$	0	3	2	5	4	7	6	9	8	11	10	13	12	13	$g_B(k)$	0	1	0	3	2	5	4	7	6	9	8	11	10	13

Applying the pattern from Table *2* to Figure 6 and Figure 7, we obtain Figure 9 and Figure 8 correspondingly, from which we can see the characteristic sidestepping.

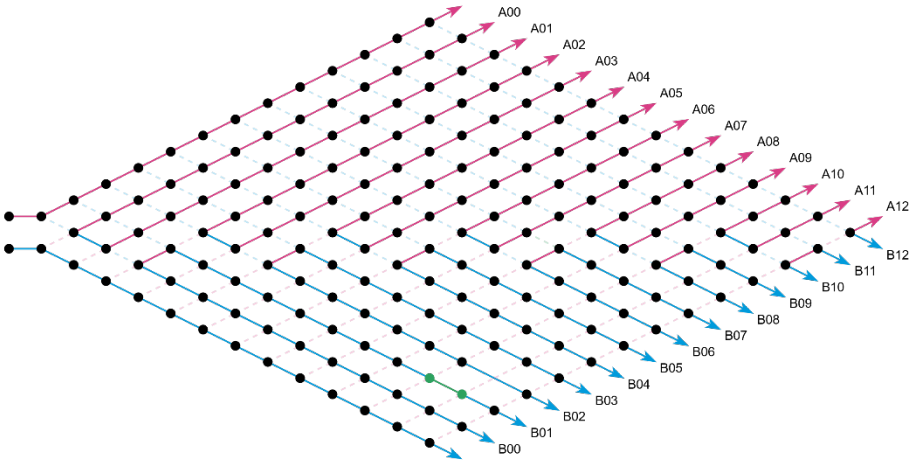

Figure 8: Pattern of applied to Figure 7. Green Segment of curve B_{01} is preserved (1).

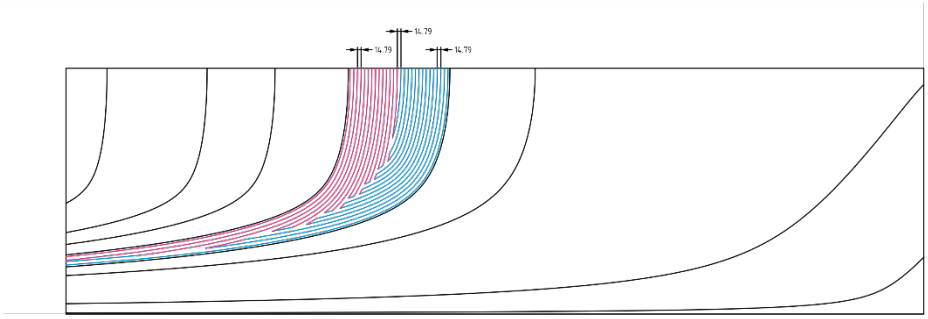

Figure 9: Illustration of the final toolpath with the following characteristics: complete coverage of the area between the trajectories T_A and T_B, no local over-extrusion by consistent distance between toolpaths, no gaps, and toolpath finish at the same side it starts.

It should be noted that the evaluation of $g_A(k)$ and $g_B(k)$ works only for odd values of n. For even values of n, round up n to the nearest odd integer by adding 1, evaluate $g_A(k)$ and $g_B(k)$ for $n+1$, construct the pattern, and remove the last row and column, see Table 3.

Table 3: Modification of the pattern for even values of $\ddot{n} = 12$ by removing the last row and the last column of the pattern from Table 2.

	B_{00}	B_{00} - B_{01}	B_{01} - B_{02}	B_{02} - B_{03}	B_{03} - B_{04}	B_{04} - B_{05}	B_{05} - B_{06}	B_{06} - B_{07}	B_{07} - B_{08}	B_{08} - B_{09}	B_{09} - B_{10}	B_{10} - B_{11}	B_{11}		A_{00}	A_{00} - A_{01}	A_{01} - A_{02}	A_{02} - A_{03}	A_{03} - A_{04}	A_{04} - A_{05}	A_{05} - A_{06}	A_{06} - A_{07}	A_{07} - A_{08}	A_{08} - A_{09}	A_{09} - A_{10}	A_{10} - A_{11}	A_{11}
A_{00}	0	1	1	1	1	1	1	1	1	1	1	1	1	B_{00}	0	1	0	1	1	1	1	1	1	1	1	1	1
A_{01}	0	1	1	1	1	1	1	1	1	1	1	1	1	B_{01}	0	0	0	1	1	1	1	1	1	1	1	1	1
A_{02}	0	1	0	1	1	1	1	1	1	1	1	1	1	B_{02}	0	0	0	1	0	1	1	1	1	1	1	1	1
A_{03}	0	0	0	1	1	1	1	1	1	1	1	1	1	B_{03}	0	0	0	0	0	1	1	1	1	1	1	1	1
A_{04}	0	0	0	1	0	1	1	1	1	1	1	1	1	B_{04}	0	0	0	0	0	1	0	1	1	1	1	1	1
A_{05}	0	0	0	0	0	1	1	1	1	1	1	1	1	B_{05}	0	0	0	0	0	0	0	1	1	1	1	1	1
A_{06}	0	0	0	0	0	1	0	1	1	1	1	1	1	B_{06}	0	0	0	0	0	0	0	1	0	1	1	1	1
A_{07}	0	0	0	0	0	0	0	1	1	1	1	1	1	B_{07}	0	0	0	0	0	0	0	0	0	1	1	1	1
A_{08}	0	0	0	0	0	0	0	1	0	1	1	1	1	B_{08}	0	0	0	0	0	0	0	0	0	1	0	1	1
A_{09}	0	0	0	0	0	0	0	0	0	1	1	1	1	B_{09}	0	0	0	0	0	0	0	0	0	0	0	1	1
A_{10}	0	0	0	0	0	0	0	0	0	1	0	1	1	B_{10}	0	0	0	0	0	0	0	0	0	0	0	1	0
A_{11}	0	0	0	0	0	0	0	0	0	0	0	1	1	B_{11}	0	0	0	0	0	0	0	0	0	0	0	0	0

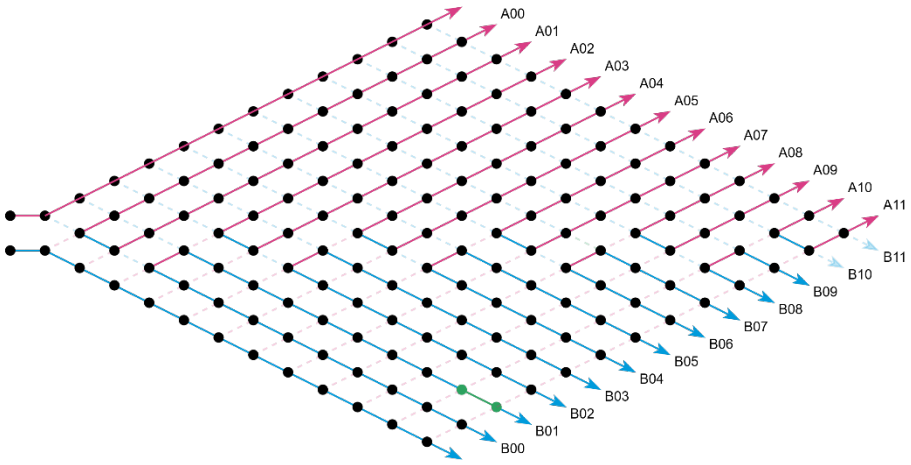

Figure 10: Pattern of Table 3 applied to Figure 7 (excluding A_{12}/B_{12}). The only difference is the intersection of the last two curves.

4.1 Case Study

The previously described algorithm is applied to the initial example in Figure 1. It can be shown that the complete computational domain can be covered with a single, continuous toolpath, see Figure 11. This is especially advantageous for extrusion-based 3DCP if there is no further material discharge mechanism at the end effector and a pump stop is only noticed with a delay at the end effector. Figure 12 shows the results of the naïve method, which yields a toolpath not suitable for 3DCP as outlined in the caption.

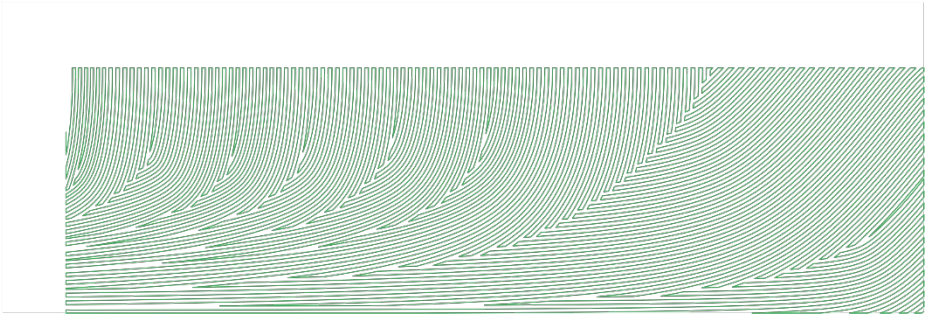

Figure 11: Continuous toolpath following the principal stress pattern, with reduced sharp angles and no gaps, equidistant spacing of toolpaths between two trajectories T_A and T_B.

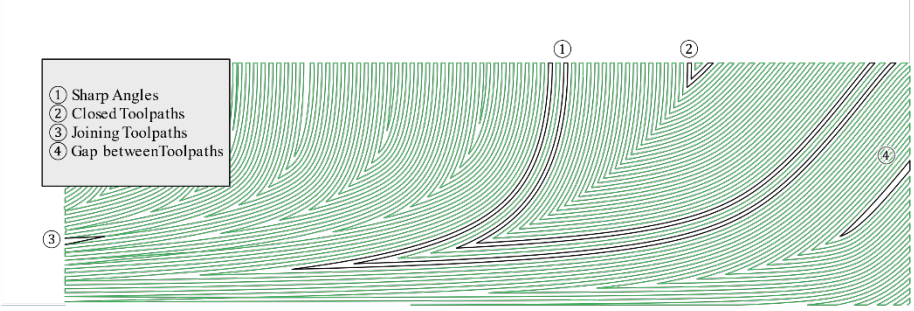

Figure 12: Toolpath based on the naïve variant. This results in many sharp angles, curves that are closed in on themselves and curves that are too far apart, as well as unfavorable joining of partial toolpaths.

5. Conclusion & Outlook

It can be concluded that by relaxing given nozzle widths and accepting uniform over-extrusion between $\mathrm{T_A}$ and $\mathrm{T_B}$, a toolpath suitable for 3DCP can be derived. The developed methodology, shown in Figure 11 shows promising initial results compared to the naïve method, shown in Figure 12. If the algorithm is allowed an offset dimension smaller than the nozzle diameter and enforces an even number of offset curves, a toolpath can be planned that can be continuously processed by an industrial robot used for 3DCP. Incorporating a rotationally symmetrical nozzle not only simplifies robot programming through the specification of $\mathrm{X, Y, Z}$ coordinates but also eliminates the risk of hose entanglement, as the print head does not need to rotate.

Further improvements to the algorithm proposed herein will include the determination of the optimal set of adjacent trajectories $\mathrm{T_A}$ and $\mathrm{T_B}$ and the determination of one single $\mathrm{w_{eff}} \leq \mathrm{w_{nom}}$ for the complete computational domain Ω.

Data availability statement

The full code is currently not published. In case of interest, the corresponding au-thor will provide the data upon reasonable request.

Competing interests

The authors declare no competing interests.

Funding

This research was funded by the Deutsche Forschungsgemeinschaft (DFG, German Research Foundation) – Project Number 423969184 – SPP 2187.

Acknowledgement

If you want to acknowledge persons or institutions you can do so here.

References

[1] G. Ma, R. A. Buswell, W. R. L. da Silva, L. Wang, J. Xu, and S. Z. Jones, "Tech-nology Readiness: A Global Snapshot of 3D Concrete Printing and the Frontiers for Development,", Cem. Concr. Res., vol. 156, 2022, doi: 10.1016/j.cemconres.2022.106774.

[2] D. Lowke, A. Vandenberg, A. Pierre, A. Thomas, H. Kloft, and N. P. Hack, "In-jection 3D Concrete Printing in a Carrier Liquid: Underlying Physics and Appli-cations to Lightweight Space Frame Structures,", Cem. Concr. Compos., vol. 124, 2021, doi: 10.1016/j.cemconcomp.2021.104169.

[3] N. P. Hack, I. Dressler, L. Brohmann, S. Gantner, D. Lowke, and H. Kloft, "In-jection 3D Concrete Printing (I3DCP): Basic Principles and Case Studies,", Ma-terials, early access. doi: 10.3390/ma13051093.

[4] T. T. Le et al., "Hardened Properties of High-Performance Printing Concrete,", Cem. Concr. Res., vol. 42, no. 3, pp. 558–566, 2012, doi: 10.1016/j.cemconres.2011.12.003.

[5] V. Naidu Nerella, S. Hempel, and V. Mechtcherine, "Effects of Layer-Interface Properties on Mechanical Performance of Concrete Elements Produced by Ex-trusion-Based 3D-Printing,", Constr. Build. Mater., vol. 205, pp. 586–601, 2019, doi: 10.1016/j.conbuildmat.2019.01.235.

[6] R. J. M. Wolfs, F. P. Bos, and T. A. M. Salet, "Hardened Properties of 3D Printed Concrete: The Influence of Process Parameters on Interlayer Adhesion,", Cem. Concr. Res., vol. 119, pp. 132–140, 2019, doi: 10.1016/j.cemconres.2019.02.017.

[7] A. V. Rahul, M. Santhanam, H. Meena, and Z. Ghani, "Mechanical Characteri-zation of 3D Printable Concrete,", Constr. Build. Mater., vol. 227, 2019, doi: 10.1016/j.conbuildmat.2019.116710.

[8] C. Joh, J. Lee, T. Q. Bui, J. Park, and I.-H. Yang, "Buildability and Mechanical Properties of 3D Printed Concrete,", Materials, early access. doi: 10.3390/ma13214919.

[9] M. Meurer and M. Claßen, "Mechanical Properties of Hardened 3D Printed Concretes and Mortars: Development of a Consistent Experimental Characteri-zation Strategy,", Materials, early access. doi: 10.3390/ma14040752.

[10] V. Mechtcherine et al., "Integrating Reinforcement in Digital Fabrication with Concrete: A Review and Classification Framework,", Cem. Concr. Compos., vol. 119, 2021, doi: 10.1016/j.cemconcomp.2021.103964.

[11] V. Mechtcherine et al., "A Roadmap for Quality Control of Hardening and Hardened Printed Concrete,", Cem. Concr. Res., vol. 157, 2022, doi: 10.1016/j.cemconres.2022.106800.

[12] S. C. Figueiredo et al., "Mechanical Behavior of Printed Strain Hardening Cementitious Composites,", Materials, early access. doi: 10.3390/ma13102253.
[13] P. Lauff and O. Fischer, "Effizienter Ultrahochleistungsbeton mit innovativer trajektorienorientierter „Bewehrung“,", ce papers, vol. 3, no. 2, pp. 82–88, 2019, doi: 10.1002/cepa.976.
[14] S. Gantner, P. Rennen, T. N. Rothe, C. Hühne, and N. P. Hack, "Core Winding: Force-Flow Oriented Fibre Reinforcement in Additive Manufacturing with Con-crete," in Third RILEM International Conference on Concrete and Digital Fab-rication: Digital Concrete 2022, Loughborough, UK, R. A. Buswell, A. Blanco, S. Cavalaro, and P. Kinnell, Eds., vol. 37, 2022, pp. 391–396, doi: 10.1007/978-3-031-06116-5_58.
[15] F. P. Bos, Z. Y. Ahmed, R. J. M. Wolfs, and T. A. M. Salet, "3D Printing Concrete with Reinforcement," in High Tech Concrete: Where Technology and Engineer-ing Meet, Maastricht, NL, D. A. Hordijk and M. Luković, Eds., 2017, pp. 2484–2493, doi: 10.1007/978-3-319-59471-2_283.
[16] V. Mechtcherine, A. Michel, M. Liebscher, and T. Schmeier, "Extrusion-Based Additive Manufacturing with Carbon Reinforced Concrete: Concept and Feasi-bility Study,", Materials, early access. doi: 10.3390/ma13112568.
[17] L. Demont, N. Ducoulombier, R. Mesnil, and J.-F. Caron, "Flow-Based Pultrusion of Continuous Fibers for Cement-Based Composite Material and Additive Manufacturing: Rheological and Technological Requirements,", Compos. Struct., vol. 262, 2021, doi: 10.1016/j.compstruct.2021.113564.
[18] M. Bi et al., "Continuous Contour-Zigzag Hybrid Toolpath for Large Format Additive Manufacturing,", Addit. Manuf., vol. 55, 2022, doi: 10.1016/j.addma.2022.102822.
[19] X. Chen, G. Fang, W.-H. Liao, and C. C. Wang, "Field-Based Toolpath Generation for 3D Printing Continuous Fibre Reinforced Thermoplastic Composites,", Addit. Manuf., vol. 49, p. 102470, 2022, doi: 10.1016/j.addma.2021.102470.
[20] X. Guidetti, E. C. Balta, Y. Nagel, H. Yin, A. Rupenyan, and J. Lygeros, "Stress Flow Guided Non-Planar Print Trajectory Optimization for Additive Manufac-turing of Anisotropic Polymers,", Addit. Manuf., vol. 72, p. 103628, 2023, doi: 10.1016/j.addma.2023.103628.
[21] T. Heitkamp et al., "Stress-Adapted Fiber Orientation Along the Principal Stress Directions for Continuous Fiber-Reinforced Material Extrusion,", Prog. Addit. Manuf., vol. 8, no. 3, pp. 541–559, 2023, doi: 10.1007/s40964-022-00347-x.
[22] T. Liu et al., "Stress-Driven Infill Mapping for 3D-Printed Continuous Fiber Composite with Tunable Infill Density and Morphology,", Addit. Manuf., vol. 62, p. 103374, 2023, doi: 10.1016/j.addma.2022.103374.
[23] E. Sales, T.-H. Kwok, and Y. Chen, "Function-Aware Slicing Using Principal Stress Line for Toolpath Planning in Additive Manufacturing,", J. Manuf. Pro-cess., vol. 64, pp. 1420–1433, 2021, doi: 10.1016/j.jmapro.2021.02.050.
[24] F. Wulle, "Untersuchung der belastungsgerechten Bahnplanung für das mehrachsige Schmelzschichtverfahren für Bauteile mit Zugspannungen,", 2023, doi: 10.18419/opus-13133.
[25] L. Xia, S. Lin, and G. Ma, "Stress-Based Tool-Path Planning Methodology for Fused Filament Fabrication,", Addit. Manuf., vol. 32, p. 101020, 2020, doi: 10.1016/j.addma.2019.101020.
[26] H. Zhang, Y. Yao, Y. Ma, M. Lackner, and Y. Jiang, "A 3D Printing Tool-Path Generation Strategy Based on the Partition of Principal Stress Field for Fused Filament Fabrication,", Int. J. Adv. Manuf. Technol., vol. 122, 3-4, pp. 1719–1735, 2022, doi: 10.1007/s00170-022-09957-9.
[27] B. Blagojevic and O. Sawodny, "Path Planning for Graded Concrete Element Fabrication,", Constr. Robot., 2023, doi: 10.1007/s41693-023-00096-5.
[28] L. Breseghello, H. Hajikarimian, H. B. Jørgensen, and R. Naboni, "3DLightBeam+: Design, Simulation, and Testing of Carbon-Efficient Rein-forced 3D Concrete Printed Beams,", Eng. Struct., vol. 292, p. 116511, 2023, doi: 10.1016/j.engstruct.2023.116511.

[29] L. Breseghello and R. Naboni, "Toolpath-Based Design for 3D Concrete Printing of Carbon-Efficient Architectural Structures,", Addit. Manuf., vol. 56, 2022, doi: 10.1016/j.addma.2022.102872.

[30] R. Dörrie and H. Kloft, "Force Flow Compliant Robotic Path Planning Approach for Reinforced Concrete Elements Using SC3DP," in Third RILEM International Conference on Concrete and Digital Fabrication: Digital Concrete 2022, Loughborough, UK, R. A. Buswell, A. Blanco, S. Cavalaro, and P. Kinnell, Eds., vol. 37, 2022, pp. 370–375, doi: 10.1007/978-3-031-06116-5_55.

[31] J. Liu, S. Li, K. Fox, and P. Tran, "3D Concrete Printing of Bioinspired Bouligand Structure: A Study on Impact Resistance,", Addit. Manuf., vol. 50, 2022, doi: 10.1016/j.addma.2021.102544.